Membranes
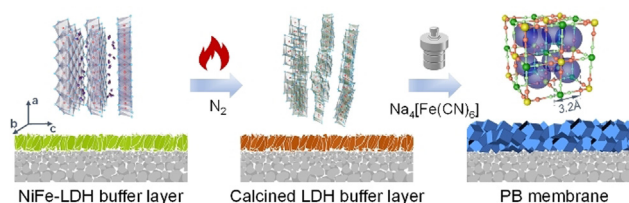
Layered Double Hydroxide-Assisted Fabrication of Prussian Blue Membranes for Precise Molecular Sieving

Qi Bian+, Mu Zhang+, Yi Liu+, Liangliang Liu+, Yang Li, Chen Wang, Gaohong He, and Yi Liu*

Dedicated to Professor Jürgen Caro on the occasion of his 70th birthday

Abstract: *Prussian Blue (PB), which was first discovered as robust blue-colored pigment in the year 1706, has shown promising prospects in disease treatment, energy conversion, water splitting, and sensing. Relying on the uniform 3.2 Å-sized pore channels as well as high stability in aqueous environments, in this study, we pioneered in situ preparation of polycrystalline PB membranes to justify their dye rejection and metal ion discrimination ability in aqueous environments. Among various factors, the introduction of calcined NiFe layered double hydroxide buffer layers on porous α-Al$_2$O$_3$ substrates was found to play a paramount role in the formation of continuous polycrystalline PB membranes, thereby leading to excellent dye rejection efficiency (> 99.0 %). Moreover, prepared PB membranes enabled discriminating different monovalent metal ions (e.g., Li+, Na+, and K+) depending on their discrepancy in Stokes diameters, showing great promise for lithium extraction from smaller-sized metal ions.*

$\mathbf{P}$russian Blue (PB), which was first discovered as robust blue-colored pigment in the year 1706, represents a coordination compound formed by combining mixed-valent iron ions with cyanide anions, while monovalent metal ions (e.g., K+) are inserted into the voids of the crystal lattice.[1] At present, PB and PB analogues (PBA) have been extensively studied and shown potential applications as oxygen evolution reaction (OER) catalysts,[2] electrode materials,[3] supercapacitors,[4] and gas adsorbents.[5] As shown in Figure 1, PB built from Fe^{II}-C≡N-Fe^{III} sequences has a regular pore size of 3.2 Å, making them superb candidates for size-based molecular sieving. Combined with the long-term structural robustness in aqueous environments, PB in the form of polycrystalline membrane is anticipated to show promising applications in nanofiltration (like dye rejection) and metal ion discrimination (like discrimination of larger-sized Li + with Stokes diameter (SD) of 0.48 nm from smaller-sized Na+ and K+ with SDs of 0.37 nm and 0.25 nm, respectively) in aqueous environments.[6] However, to date there has been no report

[*] Q. Bian,[+] M. Zhang,[+] Dr. Y. Liu,[+] Dr. L. L. Liu,[+] Y. Li, Dr. C. Wang, Prof. G. H. He, Prof. Y. Liu
State Key Laboratory of Fine Chemicals
School of Chemical Engineering, Dalian University of Technology
Linggong Road NO. 2, Ganjingzi District, Dalian 116024 (China)
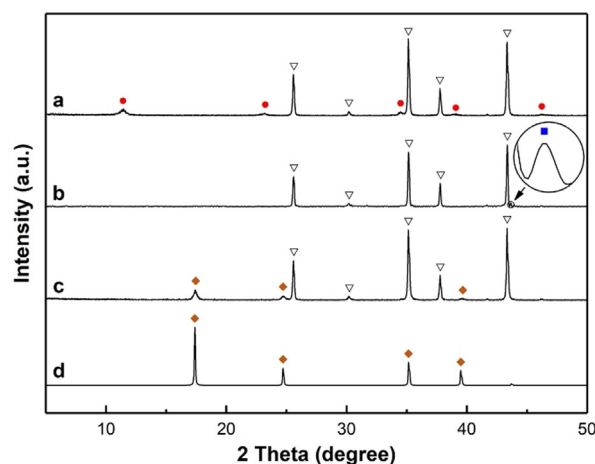E-mail: diligenliu@dlut.edu.cn

[+] These authors contributed equally to this work.

🖳 Supporting information and the ORCID identification number(s) for
ⓘD the author(s) of this article can be found under:
https://doi.org/10.1002/anie.202113662.

Figure 1. Illustration of the fabrication of continuous polycrystalline PB membrane.

on the fabrication of well-intergrown polycrystalline PB membranes due to excessively fast nucleation rate of PB grains in the bulk solutions and therefore, relatively low heterogenous nucleation density on substrate surfaces.

Surface modification of substrates with functional buffer layers represents an effective approach to enhance the heterogenous nucleation density of polycrystalline PB membranes. Layered double hydroxide (LDH), which is representative of inorganic pillared clays, has shown promising applications in catalysis,[7] adsorption,[8] anticorrosion,[9] and membrane separation.[10] Moreover, our recent study indicated that LDH-based buffer layers could serve as competent heterogenous nucleation center facilitating in situ growth of a series of well-intergrown metal-organic framework (MOF) membranes (including ZIF-7,[11] ZIF-8,[12] ZIF-67,[13] and HKUST-1[14]), relying on their rich surface functionality and flexible chemical composition. Very recently, this approach was also proven effective in preparation of well-intergrown COF (e.g., COF-LZU1) membranes with excellent gas separation performances.[15]

In this study, we developed a facile in situ growth method for preparing continuous polycrystalline PB membranes on porous α-Al$_2$O$_3$ substrates. Surface modification of the substrates with calcined NiFe-CO$_3$ LDH buffer layers, which could be facilely prepared by in situ hydrothermal growth, played a vital role in the formation of well-intergrown PB membranes. Owing to the appropriate pore aperture, prepared PB membranes exhibited excellent performances towards dye rejection and monovalent metal ion discrimination.

Initially we attempted to prepare PB membranes on bare porous α-Al$_2$O$_3$ substrates via in situ hydrothermal growth. Nevertheless, it turned out to be very difficult to form continuous PB membranes. PB crystals were only sparsely distributed on the substrate surface even under optimized synthetic conditions (shown in Figure S3), which could be attributed to the weak affinity interaction between PB grains

and bare substrate surface. Therefore, surface modification of substrates with chemically active buffer layers has become indispensable. NiFe-CO$_3$ LDH is considered as an ideal candidate considering the chemical composition similarity with PB as well as the ease of fabrication.

NiFe-CO$_3$ LDH buffer layers could be facilely in situ grown on porous α-Al$_2$O$_3$ substrates via simply immersing in aqueous solutions containing Ni(NO$_3$)$_2$·6H$_2$O, FeCl$_3$·6H$_2$O, L-ascorbic acid (LAA) and urea. As shown in Figure 2a, after hydrothermal reaction at 120°C for 24 h, uniform and closely packed 0.4 μm-thick NiFe-CO$_3$ LDH buffer layers had been formed. Cross-sectional SEM image (Figure 2b) indicated that a majority of platelet-shaped LDH grains were vertically grown on the substrates, which could be explained by the evolution selection principle developed by van der Drift.[16] The XRD pattern (Figure 3a) convincingly confirmed that prepared buffer layers indeed belonged to pure LDH phase. Moreover, the interlayer spacing was calculated to be 7.6 Å based on (003) peak position in the XRD pattern, thereby implying that carbonate anions had been intercalated in the interlayer galleries.[17]

It should be noted that addition of LAA in precursor solutions was indispensable for effective morphology control of NiFe-CO$_3$ LDH buffer layers in terms of effective reduction in surface energy of the (001) facet as revealed in previous studies.[18] As a comparative experiment, we also tried preparing NiFe-CO$_3$ LDH buffer layers in the absence of LAA. Corresponding results indicated that along with the formation of large-sized NiFe-CO$_3$ LDH aggregates in bulk solutions, only loosely packed amorphous particles instead of
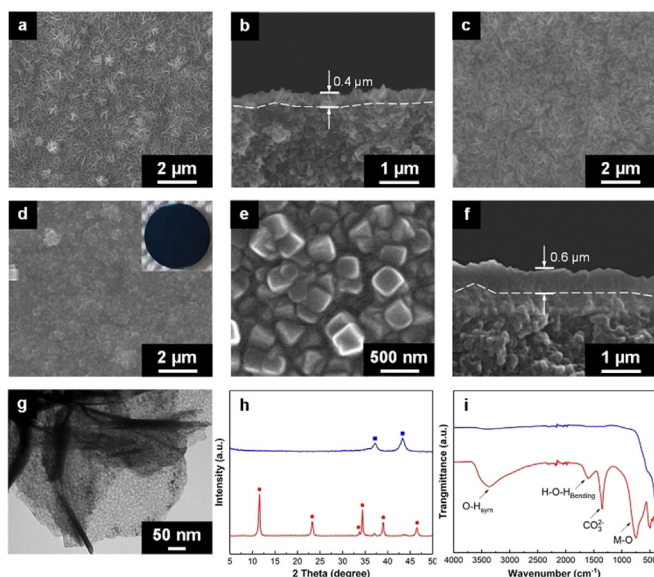

Figure 2. SEM images of the a) top and b) cross-sectional view of NiFe-CO$_3$ LDH buffer layer, c) SEM image of calcined NiFe-CO$_3$ LDH buffer layer, SEM images of the d),e) top and f) cross-sectional view of polycrystalline PB membrane, inset shows the optical photo of PB membrane on α-Al$_2$O$_3$ substrates; g) TEM image of calcined NiFe-LDH powders, h) XRD patterns and i) FT-IR spectra of pristine (red line) and calcined (blue line) NiFe-CO$_3$ LDH powders (red ● denoted diffraction peaks of NiFe-CO$_3$ LDH phase; blue ■ denoted diffraction peaks of NiO phase).

Figure 3. XRD patterns of a) NiFe-CO$_3$ LDH buffer layer, b) calcined NiFe-CO$_3$ LDH layer, c) PB membrane, and d) simulated PB powders (red ● denoted NiFe-CO$_3$ LDH phase, black ■ denoted NiO phase, orange ◆ denoted PB phase, and ▽ denoted α-Al$_2$O$_3$ phase, respectively).

crystalline NiFe-CO$_3$ LDH crystallites were attached to the substrates (shown in Figure S4).

In the next step, prepared NiFe-CO$_3$ LDH buffer layers were immersed in PB precursor solutions and kept in an oven at 120°C for 6 h. XRD and SEM results indicated that after the reaction, continuous PB membranes had been formed. Nevertheless, the SEM image at higher magnification indicated that some voids and grain boundary defects remained clearly visible in the membrane (shown in Figure S5). Fortunately, this morphological imperfection could be solved by calcinating the NiFe-CO$_3$ LDH buffer layers under controlled conditions. XRD and SEM results indicated that after calcination, although surface morphology of the buffer layers remained largely unchanged (Figure 2c), all diffraction peaks derived from pristine NiFe-CO$_3$ LDH phase had disappeared (Figure 3b), implying that buffer layers had lost their original crystallinity. Instead, a weak diffraction peak at 43.2°, which corresponded to the (200) plane of NiO phase, appeared. After hydrothermal treatment of calcined NiFe-CO$_3$ LDH buffer layer-modified substrates in aqueous solutions containing PVP, HCl and Na$_4$Fe(CN)$_6$·10H$_2$O, well-intergrown PB membranes with an average grain size of 0.4 μm and a thickness of 0.6 μm had been formed (Figure 2d–f), and all the peaks in the XRD pattern (Figure 3c) were consistent with the simulated ones (Figure 3d).

The large morphological discrepancy between PB membranes in situ grown on pristine (Figure S5) and calcined (Figure 2d) NiFe-CO$_3$ LDH buffer layer-modified α-Al$_2$O$_3$ substrates inspired us to explore further the dominant factors determining their morphology. To further exclude the interference from porous α-Al$_2$O$_3$ substrates in the XRD pattern, NiFe-CO$_3$ LDH powders sedimented at the bottom of the vessel after the hydrothermal reaction were collected and calcined under the same condition. Relevant TEM image (Figure 2g) demonstrated that platelet-shaped NiFe-CO$_3$ LDH powders had been converted to 5–10 nm-sized metal oxide nanoparticles after calcination. The XRD pattern of

calcined NiFe-CO$_3$ LDH powders (shown in Figure 2h) further confirmed that the diffraction peaks derived from pristine NiFe-CO$_3$ LDH powders had completely disappeared; alternatively, new diffraction peaks located at 37.3° and 43.2°, which could be further indexed to the (111) and (200) planes of NiO phase, were clearly resolved. The above results were in good accordance with those reported in the literature.[19]

In addition, FT-IR tests were performed to identify surface functional groups of pristine and calcined NiFe-CO$_3$ LDH powders, respectively (Figure 2i). Our experimental results indicated that compared with pristine NiFe-CO$_3$ LDH powders, there existed almost no absorption peaks for the calcined counterpart,[20] implying that it was mainly metal oxide nanoparticles (i.e., FeO$_x$ and NiO) rather than surface functional groups that contributed to the formation of well-intergrown polycrystalline PB membranes, which was due to their high reactivity derived from high surface free energy and dangling bond density which referred to the number of bonds with unsaturated electronic coordination environment per unit area on relevant crystal plane.[21] Moreover, after calcination, accompanying with the destruction of the layered structure of NiFe-CO$_3$ LDH buffer layers, the surface areas were estimated to be ≈2.5 times that of the pristine samples (Figure S6), which was anticipated to provide more sufficient exposure of active nucleation sites to precursor solutions.

It should be addressed that precisely controlling the concentrations of HCl and PVP in precursor solutions was of vital importance to tailor the morphology of polycrystalline PB membranes. On the one hand, addition of PVP surfactants in precursor solutions was necessary for maintaining an appropriate grain size.[22] An excessive amount of PVP would inevitably reduce the PB grain size, thereby leading to the generation of grain boundary defects (shown in Figure S7); on the other hand, introduction of HCl, which served as a catalyst for the hydrolysis of [Fe(CN)$_6$]$^{4-}$ anions, was indispensable for maintaining perfectly cube-shaped surface morphology. Nevertheless, an excessive amount of HCl in aqueous precursor solutions would result in severe etching of membrane surfaces (shown in Figure S8).[23]

In the next step, rejection test was conducted to evaluate the ability of prepared PB membranes in removing different types of dyes in view of its intrinsic framework robustness in aqueous environments and small pore size (3.2 Å). Three dye molecules with similar molecular weight but different chemical structure, i.e., calcein (CA, ζ-potential: −33.2 mV), congo red (CR, ζ-potential: −0.55 mV) and methylene blue (MB, ζ-potential: 2.14 mV), were deliberately selected and subjected to dye rejection test. Our experimental results (shown in Figure 4) indicated that prepared PB membranes maintained excellent rejection rates of above 99.0% for all types of dyes; moreover, it seemed that the discrepancy of separation efficiency between these dye molecules was dominated by size-exclusion effect since the values of rejection were in good agreement with their molecular sizes: MB < CA < CR (shown in Table S1). In addition, we noticed that water permeances were strongly dependent on the ζ-potential of dye molecules in aqueous solutions, which could be attributed to electrostatic interactions between PB membrane surfaces and dye
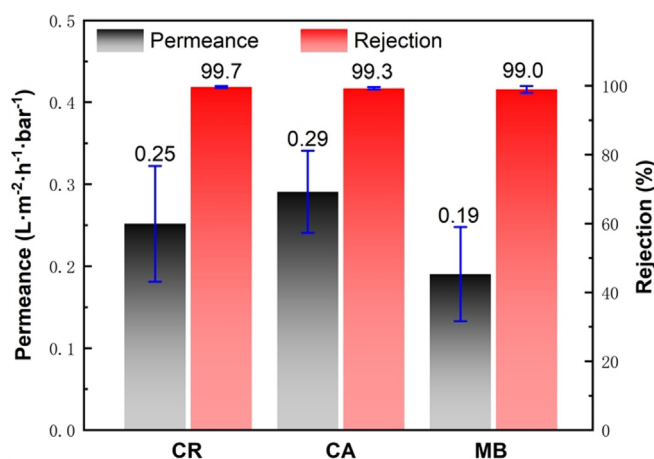

Figure 4. Dye rejection performance of PB membrane. Three different types of dyes, i.e., CR, CA and MB with the same concentration (100 mg L^{-1}) were applied in the feed side under a pressure of 2.5 bar at room temperature. Values represent means ± standard deviation for three replicates.

molecules. There was no doubt that PB membrane surfaces were negatively charged in aqueous environments, while the ζ-potential of CA, CR and MB in aqueous solutions followed the sequence: ζ$_{CA}$ (−33.2 mV) < ζ$_{CR}$ (−0.55 mV) < ζ$_{MB}$ (2.14 mV). Since the electrostatic repulsive force between PB membranes and CA molecules was the highest, correspondingly, the surface coverage of CA molecules on PB membrane surfaces was the lowest, resulting in effective avoidance of the blockage of PB pores and therefore, higher water permeances; in contrast, the electrostatic attractive force between PB membranes and MB molecules was the highest so that the surface coverage of MB molecules on PB membrane surfaces was highest, causing severe blockage of PB pores and therefore, lower water permeances.[24] Besides, the effect of operation pressure on CR molecule rejection test was investigated. As shown in Figure S9, the rejection and water permeances did not obviously change as the operation pressure increased from 1.5 to 3.5 bar. Furthermore, PB membranes showed remarkable stability during the long-term rejection test. As shown in Figure S10, no obvious decline in permeances and rejection was observed over 120 hours of operation. In addition to porous α-Al$_2$O$_3$ discs, we further succeeded in the preparation of well-intergrown PB membranes on tubular porous α-Al$_2$O$_3$ substrates (Figure S11), demonstrating the generality of this route. The cross-flow filtration test results indicated that prepared PB membranes exhibited a stable rejection to CR molecules of 99.5% with water permeances of up to 26.16 L m^{-2} h^{-1} bar^{-1} (Figure S12), which exceeded those of most membranes with comparable dye rejection in the literature (Table S2). In order to further validate the grain boundary defects of prepared PB membranes, the rejection ability towards PG molecules with smaller molecular dimensions (ca. 0.81 × 0.34 nm) was evaluated. The resulting membranes still exhibited rejection efficiency of 98.6% ± 0.15 towards PG molecules, which convincingly indicated that there existed few mesoscopic defects in PB membranes. The above experimental results

further inspired us to explore their potential in precise discrimination of monovalent metal ions with various SDs such as Li^+ (0.48 nm), Na^+ (0.37 nm) and K^+ (0.25 nm).[6b–e] For this purpose, polycrystalline PB films were fabricated on stainless steel plates in the same manner (Figure S13), and cyclic voltametric (CV) measurements were conducted in a three-electrode system with the PB film-modified stainless steel plates serving as working electrodes. All electrodes were sequentially immersed in a EC-DEC (1:1) binary solvent containing $LiPF_6$, $NaPF_6$ or KPF_6 electrolyte.

The redox peaks of the CV curve indicated the occurrence of oxidation-reduction reaction during the mutual conversion of Fe^{2+}/Fe^{3+} in the case that monovalent cations could enter the PB framework as compensating ions.[25] We kept all the starting PB films the same in all cases but screened with three possibly insertable cations of Li^+, Na^+ and K^+ with different SDs. By doing so, the nature of the host PB framework solely accounted for the variation in the redox behavior. Figure 5a
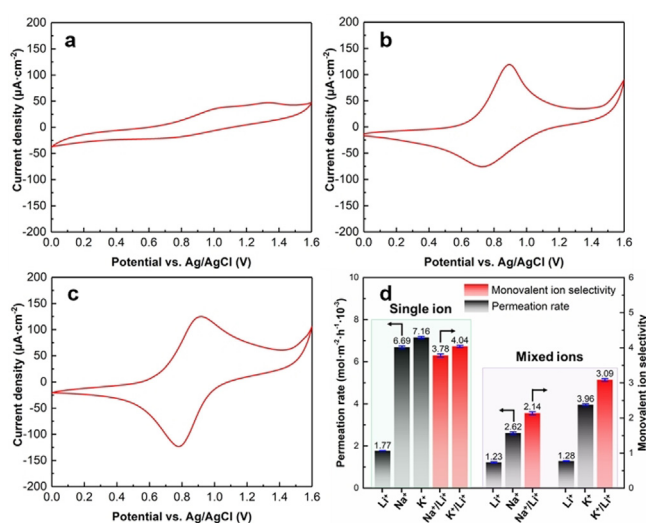
Figure 5. CV curves of PB films in a) $LiPF_6$, b) $NaPF_6$ and c) KPF_6 electrolytes, respectively; d) ionic permeation rate and monovalent ions selectivity of different ions through the polycrystalline PB membranes in single and mixed salt solution systems.

to c illustrated the CV behavior of Li^+, Na^+ and K^+, respectively. By simply exchanging the cation from Li^+ to K^+ in the electrolyte, we observed the strong dependence of cation effects on the electronic environment of the Fe^{2+}/Fe^{3+} redox center.[26] In case of the Na^+ and K^+ electrolytes, the CV curve exhibited strong and symmetrical redox peaks centered at around 0.75 V and 0.90 V vs. RHE, respectively, which indicated that Na^+ and K^+ were able to be readily embedded/dislodged in the pore channels of PB. In sharp contrast, the behavior of PB with Li^+ during CV scan was more complex, with two visibly weak and broad reactions appeared in CV curves, implying that Li^+ suffered from much higher diffusion resistance during the intercalation/deintercalation process. Based on the above results, we speculated that the distinct differences in the kinetic properties of different insertable monovalent metal ions should be directly relevant to the different SDs of the cations. For Li^+ with SD of 4.8 Å that was

much larger than the pore aperture of 3.2 Å, its diffusion in the PB channels was more sluggish as compared to Na^+ and K^+.

It is worth mentioning that although the SD of Li^+ was much larger than the pore aperture of PB, the CV redox peak of Li^+ electrolyte did not completely disappear, which could be attributed to the following factors: 1) On a mesoscopic scale, intercrystalline defects in PB films still existed, resulting in inevitable diffusion of Li^+ through these defects and therefore, the generation of redox peak; 2) On a microscopic scale, more or less there existed lattice defects within the PB framework, which would have an adverse effect on the SD-based discrimination of monovalent metal ions. To sum up, the CV results vividly confirmed that polycrystalline PB membranes held great potential for discriminating monovalent alkali cations based on their discrepancy in SDs.

Aiming at more accurate evaluation of the actual separation performances of Li^+ from other monovalent ions (e.g., Na^+ and K^+), herein ion permeation test of prepared PB membranes was conducted in a permeation cell. Figure 5d showed the permeation rates of different monovalent ions through PB membranes, where the permeation rates of K^+, Na^+, and Li^+ ions were 7.16, 6.69, and 1.77×10^{-3} mol m^{-2} h^{-1}, respectively; moreover, the single ion selectivity of Na^+/Li^+ and K^+/Li^+ reached 3.78 and 4.04, thereby clearly indicating the dominance of size-based ion sieving mechanism. Additionally, although the Li^+ permeation rate was slightly lower than its single-ion permeation rate (Figure 5d and Figure S14), prepared PB membranes still showed modest Li^+ selectivity in relevant binary ($Na^+/Li^+ = 2.14$ and $K^+/Li^+ = 3.09$) or ternary ($Na^+/Li^+ = 3.12$ and $K^+/Li^+ = 6.31$) mixed metal ion systems. To the best of our knowledge, the preparation of polycrystalline molecular sieve membranes enabling precise discrimination of monovalent metal ions has been rarely reported in the literature. Simultaneously, lithium extraction performances of the PB membranes were also comparable with the other state-of-the-art pristine 2D membranes and polymer membranes (Table S3).

To summarize, we pioneered the production of continuous polycrystalline PB membranes through facile in situ hydrothermal growth on calcined NiFe-CO$_3$ LDH buffer layers. Owing to the intrinsic framework robustness in aqueous environments and appropriate pore size, prepared PB membranes exhibited excellent rejection rates of above 99.0% for all dye molecules, irrespective of the ζ-potential values. Moreover, ion permeation test results indicated that the membranes enabled precise discrimination of various monovalent metal ions based on their discrepancy in SDs (i.e., Li^+ removal from Na^+ and K^+), thereby showing great promise for efficient lithium extraction from smaller-sized metal ions.

Conflict of Interest

The authors declare no conflict of interest.

[1] a) H.-W. Lee, R. Y. Wang, M. Pasta, S. W. Lee, N. Liu, Y. Cui, *Nat. Commun.* **2014**, *5*, 5280; b) H. J. Buser, D. Schwarzenbach, W. Petter, A. Ludi, *Inorg. Chem.* **1977**, *16*, 2704–2710; c) W.-J. Li, C. Han, G. Cheng, S.-L. Chou, H.-K. Liu, S.-X. Dou, *Small* **2019**, *15*, 1900470; d) H. C. Yi, R. Z. Qin, S. X. Ding, Y. T. Wang, S. N. Li, Q. H. Zhao, F. Pan, *Adv. Funct. Mater.* **2021**, *31*, 2006970.

[2] a) S. Pintado, S. Goberna-Ferrón, E. C. Escudero-Adán, J. R. Galán-Mascarós, *J. Am. Chem. Soc.* **2013**, *135*, 13270–13273; b) G. Yilmaz, C. F. Tan, M. Hong, G. W. Ho, *Adv. Funct. Mater.* **2018**, *28*, 1704177; c) W. Jiang, T. Wang, H. Chen, X. Suo, J. Y. Liang, W. S. Zhu, H. M. Li, S. Dai, *Nano Energy* **2021**, *79*, 105464.

[3] a) Q. N. Liu, Z. Hu, M. Z. Chen, C. Zou, H. L. Jin, S. Wang, S.-L. Chou, Y. Liu, S.-X. Dou, *Adv. Funct. Mater.* **2020**, *30*, 1909530; b) Z. Shadike, D.-R. Shi, W. Tian, M.-H. Cao, S.-F. Yang, J. Chen, Z.-W. Fu, *J. Mater. Chem. A* **2017**, *5*, 6393–6398; c) Y. Xu, S. Zheng, H. Tang, X. Guo, H. Xue, H. Pang, *Energy Storage Mater.* **2017**, *9*, 11–30.

[4] E. S. Goda, S. Lee, M. Sohail, K. R. Yoon, *J. Energy Chem.* **2020**, *50*, 206–229.

[5] S. S. Kaye, J. R. Long, *J. Am. Chem. Soc.* **2005**, *127*, 6506–6507.

[6] a) P. Gibot, M. Casas-Cabanas, L. Laffont, S. Levasseur, P. Carlach, S. Hamelet, J.-M. Tarascon, C. Masquelier, *Nat. Mater.* **2008**, *7*, 741–747; b) E. R. Nightingale, *J. Phys. Chem.* **1959**, *63*, 1381–1387; c) X. Wu, L. S. Fan, Y. Qiu, M. X. Wang, J. H. Cheng, B. Guan, Z. K. Guo, N. Q. Zhang, K. N. Sun, *ChemSusChem* **2018**, *11*, 3345–3351; d) X. Wu, M. Shao, C. Wu, J. Qian, Y. Cao, X. Ai, H. Yang, *ACS Appl. Mater. Interfaces* **2016**, *8*, 23706–23712; e) Z. Ali, B. S. Ghanem, Y. G. Wang, F. Pacheco, W. Ogieglo, H. Vovusha, G. Genduso, U. Schwingenschlögl, Y. Han, I. Pinnau, *Adv. Mater.* **2020**, *32*, 2001132.

[7] Y. Y. Wang, Y. Q. Zhang, Z. J. Liu, C. Xie, S. Feng, D. D. Liu, M. F. Shao, S. Y. Wang, *Angew. Chem. Int. Ed.* **2017**, *56*, 5867–5871; *Angew. Chem.* **2017**, *129*, 5961–5965.

[8] F. B. Dalla Nora, V. V. C. Lima, M. L. S. Oliveira, A. Hosseini-Bandegharaei, T. A. D. Burgo, L. Meili, G. L. Dotto, *J. Environ. Chem. Eng.* **2020**, *8*, 103913.

[9] L. Hao, T. T. Yan, Y. M. Zhang, X. H. Zhao, X. D. Lei, S. L. Xu, F. Z. Zhang, *Surf. Coat. Technol.* **2017**, *326*, 200–206.

[10] Y. Liu, N. Wang, J. Caro, *J. Mater. Chem. A* **2014**, *2*, 5716–5723.

[11] Y. Liu, R. Matsuda, S. Kusaka, A. Hori, Y. S. Ma, S. Kitagawa, *CrystEngComm* **2018**, *20*, 6995–7000.

[12] M. Zhang, L. Ma, L. Wang, Y. Sun, Y. Liu, *ACS Appl. Mater. Interfaces* **2018**, *10*, 2259–2263.

[13] D. Ping, X. Feng, J. Zhang, J. Geng, X. Dong, *ChemElectroChem* **2017**, *4*, 3037–3041.

[14] Z. K. Wang, L. Ge, M. R. Li, R. J. Lin, H. Wang, Z. H. Zhu, *Chem. Eng. J.* **2019**, *357*, 320–327.

[15] H. W. Fan, M. H. Peng, I. Strauss, A. Mundstock, H. Meng, J. Caro, *J. Am. Chem. Soc.* **2020**, *142*, 6872–6877.

[16] H. Chen, F. Zhang, T. Chen, S. Xu, D. G. Evans, X. Duan, *Chem. Eng. Sci.* **2009**, *64*, 2617–2622.

[17] M. Tian, C. Liu, Z. G. Neale, J. Zheng, D. Long, G. Cao, *ACS Appl. Mater. Interfaces* **2019**, *11*, 35977–35986.

[18] a) H. Ma, J. He, D.-B. Xiong, J. Wu, Q. Li, V. Dravid, Y. Zhao, *ACS Appl. Mater. Interfaces* **2016**, *8*, 1992–2000; b) F. Wang, X. Wang, *Nanoscale* **2014**, *6*, 6398–6414.

[19] a) Z. J. Zhang, D. B. Zhou, X. J. Bao, H. Z. Yu, B. Y. Huang, *Int. J. Hydrogen Energy* **2018**, *43*, 20734–20738; b) C. S. Lei, M. Pi, P. Y. Kuang, Y. Q. Guo, F. G. Zhang, *J. Colloid Interface Sci.* **2017**, *496*, 158–166.

[20] A. Guzmán-Vargas, J. Vazquez-Samperio, M. A. Oliver-Tolentino, G. Ramos-Sánchez, J. L. Flores-Moreno, E. Reguera, *Electrocatalysis* **2017**, *8*, 383–391.

[21] a) Z. W. Gao, J. Y. Liu, X. M. Chen, X. L. Zheng, J. Mao, H. Liu, T. Ma, L. Li, W. C. Wang, X. W. Du, *Adv. Mater.* **2019**, *31*, 1804769; b) S. Lee, L. C. Bai, X. L. Hu, *Angew. Chem. Int. Ed.* **2020**, *59*, 8072–8077; *Angew. Chem.* **2020**, *132*, 8149–8154.

[22] T. Uemura, S. Kitagawa, *J. Am. Chem. Soc.* **2003**, *125*, 7814–7815.

[23] a) Y. Liu, G. Wei, M. Ma, Y. Qiao, *Chem. Eur. J.* **2017**, *23*, 15991–15996; b) M. Hu, S. Furukawa, R. Ohtani, H. Sukegawa, Y. Nemoto, J. Reboul, S. Kitagawa, Y. Yamauchi, *Angew. Chem. Int. Ed.* **2012**, *51*, 984–988; *Angew. Chem.* **2012**, *124*, 1008–1012.

[24] a) C. F. Wang, J. B. Chen, X. Y. Hu, X. S. Feng, *Desalination* **2021**, *503*, 114957; b) W. Xiang, X. Y. Zhang, K. Q. Chen, J. Fang, F. He, X. Hu, D. C. W. Tsang, Y. S. Ok, B. Gao, *Chem. Eng. J.* **2020**, *385*, 123842.

[25] a) L. T. T. Kim, C. Gabrielli, H. Perrot, J. Garcia-Jareno, F. Vicente, *Electrochim. Acta* **2012**, *84*, 35–48; b) S. Jansod, T. Cherubini, Y. Soda, E. Bakker, *Anal. Chem.* **2020**, *92*, 9138–9145.

[26] L. Wang, J. Song, R. Qiao, L. A. Wray, M. A. Hossain, Y.-D. Chuang, W. Yang, Y. Lu, D. Evans, J.-J. Lee, S. Vail, X. Zhao, M. Nishijima, S. Kakimoto, J. B. Goodenough, *J. Am. Chem. Soc.* **2015**, *137*, 2548–2554.